Soft Lightweight Small-Scale Parallel Robot With High-Precision Positioning

Qin Fang, Jingyu Zhang, Danying Sun, Yanan Xue, Rui Jin, Nenggan Zheng, *Senior Member, IEEE*, Yue Wang, *Member, IEEE*, Rong Xiong, *Member, IEEE*, Zhefeng Gong, and Haojian Lu, *Member, IEEE*

***Abstract*—Small-scale (from centimeters down to micrometers) parallel robots with high precision are widely utilized in various industrial and biomedical settings, while such superiorities remain challenges for soft parallel robots (SPRs). In this work, we propose an integrated design and fabrication strategy to make up a soft lightweight (3.5 g) small-scale ($\phi 60 \times 40$ mm) parallel robot based on the dielectric elastomer actuator. Then, a hybrid model is established to describe the mapping between driving space and workspace, taking advantage of the robustness and security of the model-based method and the strong nonlinear fitting ability of the data-driven neural network method. The stiffness and workspace of the robot are analyzed. The results of trajectory tracking experiments demonstrate the accuracy and robustness of the proposed hybrid model. The average positioning error of the different trajectories is 13.4–16.6 μm. Finally, the zebrafish embryo puncture experiment is carried out to show the ability of micromanipulation. This research paves a new avenue for designing and controlling high-positioning SPRs, which is expected to be applied in the micromanipulation field.**

***Index Terms*—Dielectric elastomer actuator, micro positioning, small-scale robot, soft parallel robot (SPR).**

Manuscript received 4 November 2022; revised 20 February 2023; accepted 8 April 2023. Date of publication 10 May 2023; date of current version 15 December 2023. This work was supported in part by the Key R&D Program of Ministry of Science and Technology of China under Grant 2021ZD0114500, in part by the National Natural Science Foundation of China under Grant T2293724, in part by the Key R&D Program of Zhejiang under Grant 2022C01022, in part by the Zhejiang Provincial Natural Science Foundation of China under Grant LD22E050007, in part by the Fundamental Research Funds for the Zhejiang Provincial Universities under Grant 2021XZZX021, and in part by the Science and Technology on Space Intelligent Control Laboratory under Grant 2021-JCJQ-LB-010-13. Recommended by Technical Editor Mohammad Al Janaideh and Senior Editor Gursel Alici. *(Corresponding authors: Haojian Lu; Zhefeng Gong.)*

Qin Fang, Jingyu Zhang, Danying Sun, Yanan Xue, Rui Jin, Yue Wang, Rong Xiong, and Haojian Lu are with the State Key Laboratory of Industrial Control and Technology, and the Institute of Cyber-Systems and Control, Zhejiang University, Hangzhou 310027, China (e-mail: qinfang@zju.edu.cn; 12132011@zju.edu.cn; danyingsun@zju.edu.cn; xueyanan2020@zju.edu.cn; bbbbigrui@zju.edu.cn; wangyue@iipc.zju.edu.cn; rxiong@zju.edu.cn; luhaojian@zju.edu.cn).

Nenggan Zheng is with the Qiushi Academy for Advanced Studies, Zhejiang University, Hangzhou 310027, China (e-mail: zng@cs.zju.edu.cn).

Zhefeng Gong is with the Key Laboratory of Neurobiology, Zhejiang University School of Medicine, Hangzhou 310027, China (e-mail: zfgong@zju.edu.cn).

Color versions of one or more figures in this article are available at https://doi.org/10.1109/TMECH.2023.3270633.

Digital Object Identifier 10.1109/TMECH.2023.3270633

I. Introduction

THE parallel robots usually have higher stiffness, greater load capacity and higher accuracy compared with the classical serial robots, attracting the extensive interest of researchers and developing rapidly. The earliest parallel robot was designed by Gough in 1947, which was used to detect tire wear under various load conditions [1], [2]. In the following decades, various parallel robots have been proposed, such as delta robots [3], [4]. The advantages of parallel robots come from their closed kinematic structure. The positioning error of one kinematic chain will be reduced by other kinematic chains rather than accumulated and amplified. At the same time, the parallel configuration of multiple actuators endows the robot with sufficient rigidity to restrict external loads. In recent years, parallel robots have been widely used in various industrial applications, such as food packaging [5], machining [6], pick-and-place assembly [7], and so on.

However, the connecting rods of most parallel robots are rigid, making it unsuitable for applications requiring high biocompatibility. Some control methods could endow these robots with compliance [8], [9], but they are limited to use in special scenarios. In contrast, soft parallel robots (SPRs) composed of soft materials or flexible links have intrinsic compliance to be used in restricted or interactive environments [10], [11], [12], [13], [14].

Currently, a variety of SPRs have been developed. Yang et al. [15] developed a pneumatic robot, which is composed of three silicone chambers to achieve parallel configuration. Jiang et al. [16] developed a planar parallel robot based on the combination of tendon-driven continuum link and rigid link, which has a large workspace and high repeated positioning accuracy. Li et al. [17] used shape memory alloy (SMA) to develop a soft parallel arm made of soft silicone, and it has good operation and movement ability. Webster III and Jones [18] developed a 3-DOF soft parallel drawing robot employed with three tube-type dielectric elastomer actuators (DEAs). Godage et al. [19] proposed a SPR based on three linear DEAs with springs inside, which can achieve horizontal, vertical, and circular motions for the application of robotic eyeballs. However,

currently developed SPRs typically have relatively large sizes and weights and have submillimeter positioning accuracy. It is still challenging to design a 3-DOF SPR with the advantages of small scale, lightweight, and high precision at the same time.

On the other hand, considering the complex coupling between material nonlinearity and the kinematic chains of SPRs, the modeling and control face great challenges. The modeling methods could be roughly divided into three categories. The first is the geometric model. The shape of the robot skeleton is fitted by piecewise constant curvature (PCC) approximation [20], modal shape function approximation [21], Bessel curve approximation [22], and other methods, regardless of the materials and driving characteristics. Due to its high computation efficiency, it is widely used on various occasions requiring real-time control [23]. The second is the continuum model, such as the Cosserat model [24] and Euler–Bernoulli beam model [25], which considers the coupling of elastic force and various constraints and can accurately describe the deformation of the robots. However, due to the almost infinite degrees of freedom of the SPRs, it is difficult to be applied to the actual robot control due to the low computation efficiency. The third is the data-driven model, which learns the hidden rules from large amounts of data (input and output) without the guidance of physical models and has received a lot of attention in recent years [26]. The neural network [27] model is the most commonly used approximate mapping model. However, it is difficult to adapt to the time-varying complex environment, which limits its use.

In this article, we developed a soft lightweight small-scale parallel robot composed of three symmetrically distributed DEAs based on the integrated design and fabrication strategy. A data-driven method based on the neural network is adopted to analyze the electrodeformation characteristics of DEAs. By the kinematic model of the robot, the mapping from the driving space (input voltage) to the task space (position of the robot end effector) is established. In addition, we also carried out trajectory tracking experiments and micromanipulation experiments to verify the reliability of the model and the overall motion performance of the robot. The contribution of this work can be summarized as follows.

1) An integrated design and fabrication strategy of the 3-DOF SPR is proposed. The robot is composed of three DEAs and has a lightweight and compact structure.
2) Taking advantage of the robustness of the model-based method and the strong nonlinear fitting ability of the data-driven method, a control strategy is proposed to achieve high-precision positioning based on the hybrid model.
3) The proposed robot achieves micron-level control accuracy as well as micromanipulation capabilities, as demonstrated in trajectory tracking and zebrafish embryo puncture experiments.

The rest of this article is organized as follows. Section II describes the integrated design and fabrication strategy to make up the SPR. In Section III, a hybrid model and an open-loop controller of the robot are proposed to achieve high positioning accuracy. In Section IV, the trajectory tracking experiments and zebrafish embryo puncture experiments are carried out to analyze the performance of the robot. Finally, Section V concludes this article.

TABLE I
STRUCTURAL PARAMETERS OF THE SUPPORTING FRAME

Parameter	Value	Parameter	Value
L	196 mm	d	5 mm
H	70 mm	e	10 mm
a	50 mm	h	10 mm
b	50 mm	r	10 mm
c	2 mm	t	0.188 mm

II. INTEGRATED DESIGN AND FABRICATION

This section presents an integrated design and fabrication strategy to make up the SPR. Conventional SPRs tend to first process multiple actuators, and then, assemble them through the output stage to achieve a parallel configuration. The process is cumbersome and prone to greater processing errors and assembly errors. In contrast, our proposed design method achieves the fabrication and assembly of three DEAs simultaneously. The robot has an ultralightweight, compact structure, and a simplified manufacturing process.

To obtain the DEAs with superior performance, the manufacturing materials are seriously considered. The selection criterion of the dielectric elastomer (DE) is that the material should be soft enough to produce large deformation. The selection criteria of electrodes are low stiffness, lightweight, good adherence (not easy to slip off from the DE membrane), and maintaining high conductivity when the DE membrane deforms. These criteria for selecting materials listed previously can help increase the deformation ability of DEAs.

As for dielectric elastomer, the VHB material provides several benefits over silicone membrane material in terms of low price, good adhesion, and easy fabrication, so we choose VHB 4910 (3 M Company, USA) with an initial thickness of 1 mm as the DE membrane. And we chose carbon grease (MG chemicals, USA) as the electrode. As for flexible supporting structures, a high bending modulus will increase the deformation resistance, but if the bending modulus is too low, the actuator will quickly shrink and will not be capable of achieving the desired configuration. As a result, we choose the PET film with a thickness of $t = 0.188$ mm as the supporting frame.

After selecting the materials for the main structures, the fabrication process of the SPR can be started, as illustrated in Fig. 1(a). The PET supporting frame needs to be cut into a preset shape on the laser cutter, and the structural parameters are shown in Table I. We design the electrode area, hollow area, and bonding area on the flexible supporting structure. The shape of the electrode area is rectangular, and rounded corners are designed to reduce concentrated stress. The function of the hollowed-out area is to disperse the three actuators and reduce the interaction of the three actuators. Four minor marks are designed on the bonding area for accurate assembly of the robot. Then, the VHB membrane is prestretched at the rate of $300\% \times 300\%$ and is put on the clean bench for about six hours.

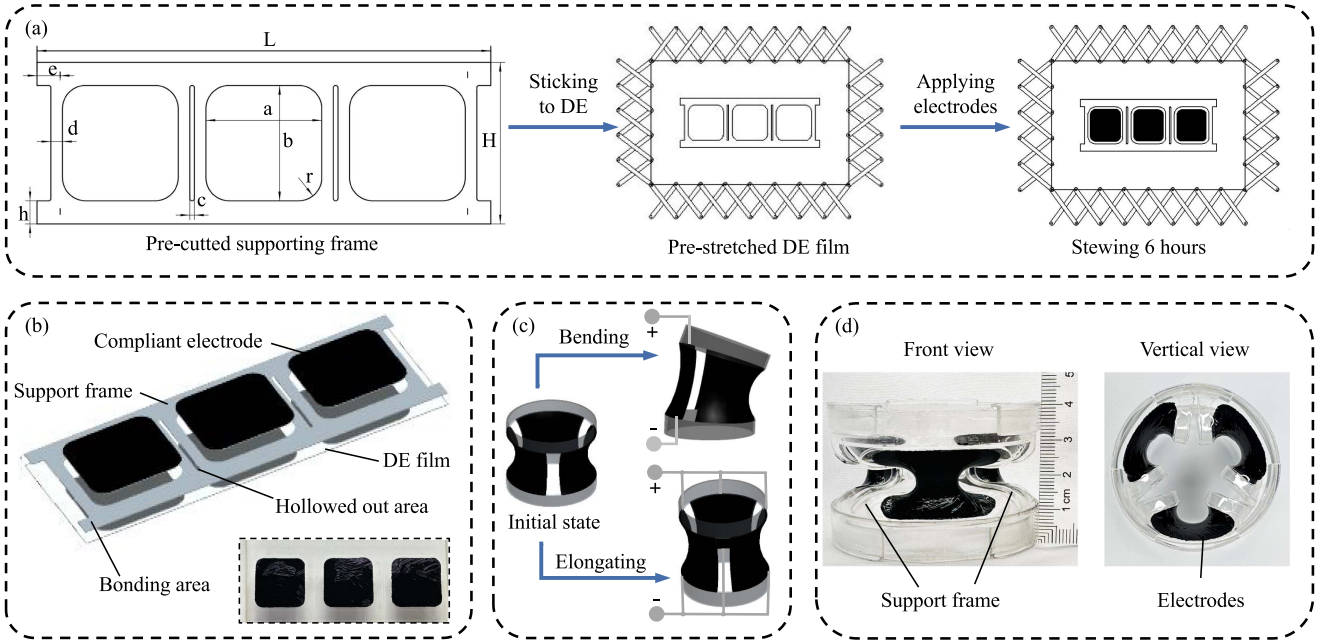

Fig. 1. Design, manufacturing, and driving principle of the SPR. (a) Manufacturing process of the SPR with the structural parameters of the supporting frame. (b) Structural composition diagram of the SPR. (c) Three modes of the SPR and deformation principle. (d) Photos of the SPR with visual reference.

Prestretching can suppress the electromechanical instability and alleviate the high viscoelasticity of the DE membrane, which is the main reason for the SPR to obtain fast response speed and stable strain under an external electric field. Then, the electrode mask is necessary for machining standard shape electrodes. A laser cutter cuts the electrode mask on the release paper. It is worth noting that there should be a distance of 2–3 mm from the edge of the electrode to the edge of the supporting frame because a large strain will occur at the edge when a high voltage is loaded. After confirming that the supporting frame is well bonded with the DE membrane, carefully cover the mask on the supporting frame, coat the carbon grease electrode, and remove the mask to obtain an electrode with a predesigned shape [the photo is shown in Fig. 1(b)]. Cutting the DE membrane in the hollow areas, and then, the three actuators will be separated. After carefully connecting the bonding area along with the minor preset marks, three actuators are evenly distributed along the circumferential direction of the robot. The front view and top view photos of the robot are shown in Fig. 1(d).

When high voltage is applied, the saddle-shaped DEA expands gradually, increasing the length of the actuator, and then, the whole robot bends. When high voltage is applied to the three DEAs simultaneously, the SPR elongates along its axes, as shown in Fig. 1(c). Theoretically, the robot could bend in any direction by adjusting the voltage on the three actuators. The frequency of elongation or bending of the robot depends on the driving voltage frequency and the DE membrane's material characteristics. To the best of our knowledge, the 3-DOF SPR based on the DEAs with lightweight and small scale is proposed for the first time. Next, we will carry out kinematic modeling of the robot.

III. Hybrid Modeling and Control Method

A. Learning-Based Electromechanical Modeling

It is necessary to characterize the electrical deformation ability of DEAs. Most of the previous research on the electric deformation of DEAs is based on the nonlinear large deformation theory of soft materials and the electromechanical coupling characteristics between the dielectric elastomer and supporting structure. However, it is difficult to accurately predict the effective output deformation of the actuator due to the following factors.

1) The complex structure and nonuniform deformation: The DE membrane forms a complex spatial structure due to the synergistic interplay between the elastic supporting frame and the electric field. At the same time, the strain distribution across the DE membrane surface is heterogeneous, with the peripheral strain of the DE membrane surpassing the strain at the center [28].
2) Material nonlinearity: The DE material demonstrate a highly nonlinear behavior [29], characterized by a substantial increase in elastic modulus as strain increases.
3) Electric field nonlinearity: As stretch rate increases, the relative permittivity of DE material decreases [30], and the uneven thickness of carbon grease electrodes may further contribute to a nonuniform electric field distribution.
4) Electromechanical coupling: There is a strong coupling between electrical and mechanical properties. The external electric fields induce deformation in the thin DE membrane and the support frame, which in turn affects the distribution of electric fields, further exacerbating the nonlinearity of DEA [31].

In summary, considering the complex electromechanical deformation of DEAs, developing a precise analytical model for DEAs remains challenging. Consequently, we chose to employ the learning-based method to model the electromechanical deformation behavior of DEAs. A neural network model is utilized to characterize the mapping relationship, circumventing the need to consider the mechanical and electrical properties of the DE membrane, support frame and compliant electrodes, and has been demonstrated to be accurate and efficient in subsequent experimental verification.

A typical neural network framework usually includes an input layer, hidden layers, and an output layer. The nonlinearity of neural networks is mainly reflected in neurons. Each neuron contains the weight w_i and bias b as well as an activation function σ. The output y of a neuron satisfies the following equation:

$$y = \sigma\left(b + \sum_{i=1}^{n} x_i w_i\right) \tag{1}$$

where x_i represents the neuron input.

For the SPR, the input of the neural network is the elongation of DEAs and the output is the actuation voltage. Before training the neural network model, the dataset was divided into the training set, verification set, and test set by the ratio of 0.7: 0.15: 0.15. The optimization algorithm is Levenberg–Marquardt, the nonlinear activation function is the sigmoid function, and the training loss mean squared error (MSE) is as follows:

$$\mathrm{MSE} = \frac{1}{m}\sum_{i=1}^{m}\left(V_i - \overline{\mathrm{V}}_i\right)^2 \tag{2}$$

where V_i is the actual voltage, and $\overline{\mathrm{V}}_i$ is the predicted voltage by the neural network.

We make the following assumptions: The first is that the three DEAs have almost consistent electromechanical characteristics. The second is that the electrodeformation model of DEAs does not change with the deformation of the robot. When applying the same voltage to the three DEAs at the same time, the upper plane of the robot will remain horizontal during the elongation process. The elongation is acquired by a high-precision laser displacement sensor (HG-C1030, Panasonic Industry (China) Co., Ltd., Shanghai, China) with a resolution of 10 μm and a dynamic range of $\pm$5 mm. It is noteworthy that in the process of collecting electrodeformation data, a thin cap (2.5 g) is placed on the robot for reflecting the laser and a marked paper sheet is placed on the cap for subsequent trajectory tracking experiments.

In order to further improve the generalization ability of neural networks, the neural network with different numbers of hidden neurons was trained over 50 times, respectively. The root means square error (RMSE) and the regression coefficient R were calculated and compared, as shown in Table II. It is observed that the training error decreases, and then, increases with the increase in the number of neurons. This can be attributed to the increasing complexity of the neural network, which eventually leads to overfitting. Therefore, it is of great significance to select the appropriate number of neurons. By the results, a neural network comprising ten hidden neurons is chosen, given its minimal RMSE of 0.6332 V, and its training results are detailed in Section IV.

TABLE II
TRAINING RESULTS OF DIFFERENT NUMBER OF HIDDEN NEURONS

Neurons	$\mathrm{RMSE}_{\min}(V)$	$\mathrm{RMSE}_{\mathrm{mean}}(V)$	$\mathrm{RMSE}_{\max}(V)$	$\mathrm{R}_{\mathrm{mean}}$
4	0.6588	0.6611	0.6663	0.999890
6	0.6496	0.6535	0.6626	0.999891
8	0.6458	0.6580	0.6935	0.999894
10	0.6332	0.6519	0.6797	0.999896
12	0.6395	0.6595	0.7176	0.999893
14	0.6395	0.6595	0.6986	0.999892
16	0.6458	0.6708	0.7036	0.999887

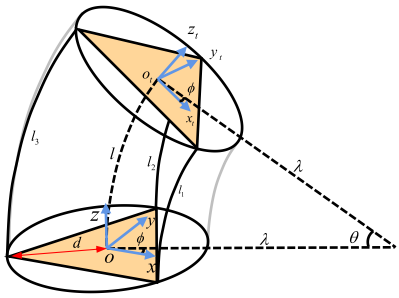

Fig. 2. Diagram of kinematic model of the SPR.

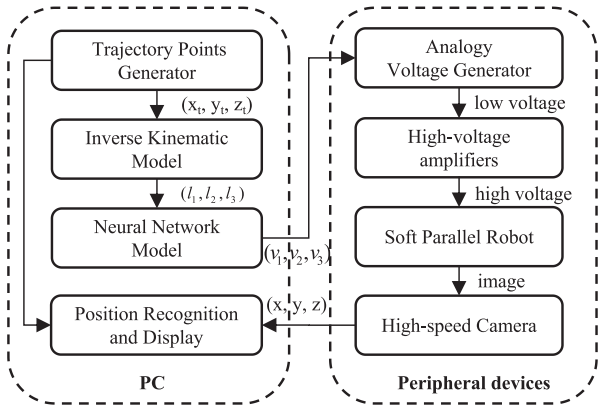

Fig. 3. Control strategy of the SPR.

B. Kinematic Modeling

After obtaining the mapping relationship between the actuation voltage and the elongation of DEAs, the kinematic model between the elongation and the motion of the center point on the top plane of the SPR is necessary to be derived. According to Fig. 2, three DEAs are fixed to the support frame at a radius d from the center at the distribution of $2\pi/3$ radian. Due to the restricted arrangement of the DEAs, the robot either exhibited pure extension or curved arcuately when a driving voltage is applied. The configuration space is defined by three spatial parameters: circle radius $\lambda \in (0, \infty)$, bending angle $\theta \in [-\pi, \pi]$, and the angle of the bending plane with respect to the X-axis, $\phi \in [0, 2\pi)$. The lengths of the three actuators are denoted as l_1, l_2, and l_3, respectively.

First, we establish the robot coordinate systems as shown in Fig. 3. The $\{OXYZ\}$ reference frame is fixed on the center of the bottom plane of the SPR, and the $\{O_tX_tY_tZ_t\}$ reference

frame is fixed on the center of the top plane. The transformation between the two reference frames could be obtained by the following steps. At first, rotate the $\{OXYZ\}$ reference frame by ϕ along the Z-axis. Next, translate the reference frame by λ along the *X*-axis. Next, rotate the new reference frame by θ along the *Y*-axis. Finally, rotate the coordinate system in the opposite direction of the first two steps, and the transformation is finished. By these steps, the original reference frame $\{OXYZ\}$ is coincident with the coordinate system $\{O_tX_tY_tZ_t\}$. This process could be described as follow:

$$\begin{aligned}\mathbf{T}_c(\boldsymbol{q}) &= \mathbf{R}_Z(\phi)\,\mathbf{P}_X(\lambda)\,\mathbf{R}_Y(\theta)\,\mathbf{P}_X(-\lambda)\,\mathbf{R}_Z(-\phi)\\ &= \begin{bmatrix}\mathbf{R}_c(\boldsymbol{q}) & \boldsymbol{p}_c(\boldsymbol{q})\\ \mathbf{0}_{1\times3} & 1\end{bmatrix}\end{aligned} \tag{3}$$

where $\mathbf{R}_Z \in SO(3)$, $\mathbf{R}_Y \in SO(3)$ are homogeneous rotation matrix, respectively, along the *Z*- and *Y*-axes, $\mathbf{P}_X \in \mathbb{R}$ is the homogeneous translation matrix along the *X*-axis, $\mathbf{R}_c \in SO(3)$ and $\boldsymbol{p}_c \in \mathbb{R}^3$ are the rotational and translation components of the transformation matrix $\mathbf{T}_c$, and $\boldsymbol{q} = \{\lambda, \phi, \theta\}$ is the spatial curve parameters unnumbered equation shown at the bottom of this page.

Finally, we could solve the complete transformation matrix $\mathbf{T}_c$. The aforementioned transformation matrix describes the mapping relationship between the spatial curve parameters and the pose of the center on the top plane of the robot.

In order to intuitively describe how the position of the top plane is influenced, we also need to establish the relationship between the lengths of DEAs (l_1, l_2, l_3) and the spatial configuration parameters $\boldsymbol{q}$. Based on the PCC model, the spatial configuration parameters of the robot can be solved by the following formulas.

$$l = \frac{1}{3}(l_1 + l_2 + l_3) \tag{4}$$

$$\phi = \tan^{-1}\left(\frac{\sqrt{3}(l_3 + l_1 - 2l_2)}{3(l_3 - l_1)}\right) \tag{5}$$

$$\lambda = \frac{d(l_1 + l_2 + l_3)}{2\sqrt{l_1^2 + l_2^2 + l_3^2 - l_1l_2 - l_1l_3 - l_2l_3}} \tag{6}$$

$$\theta = l/\lambda. \tag{7}$$

Through the forward kinematics established previously, we can obtain the position of center on the top plane of the robot according to the lengths of DEAs. Furthermore, we derive the inverse kinematics of the robot as follows:

$$\phi = \arctan\frac{y}{x} \tag{8}$$

$$\lambda = \frac{x^2 + y^2 + z^2}{2\sqrt{x^2 + y^2}} \tag{9}$$

$$\theta = \arccos\left(\frac{\lambda - \sqrt{x^2 + y^2}}{\lambda}\right) \tag{10}$$

$$l_i = l - \theta d \cdot \cos\left(\phi + \frac{\pi}{6} - \frac{2(i-1)}{3}\pi\right) \tag{11}$$

where $l_i, i = 1, 2, 3$ represents the length of the *i*th DEA.

With the aforementioned equation, we could quickly compute the length of each DEA by the desired position of the robot center.

To sum up, in Section III-A, we obtain the mapping relationship between the elongation of DEA and the driving voltage by the electrodeformation model. In Section III-B, the forward and inverse kinematics between the lengths of the DEAs and the position coordinates of the robot are established. Combining the aforementioned two models, we can solve the lengths of the DEAs by the end position, and then, get the corresponding driving voltage. This is the foundation for controlling the robot to track desired trajectories accurately.

C. Control Strategy

As shown in Fig. 3, the control strategy of the SPR is designed. Through the user-defined interface, we can select different desired trajectories. The trajectory coordinate generator is used to generate the dense coordinate sequence of the desired trajectory (x_t, y_t, z_t) in the workspace. Then, the elongation and the length of the three actuators (l_1, l_2, l_3) could be solved by the inverse kinematic model. According to the neural network model, the related analogy control voltages could be obtained. Next, the voltage generator provides the voltage sequence (v_1, v_2, v_3) and amplified by the high-voltage amplifiers. The high control voltages are applied to the SPR to obtain the desired motion. With the high-speed camera, the motion trajectory of the robot $(\mathrm{x}, \mathrm{y}, \mathrm{z})$ could be captured and shown with the desired trajectory (x_t, y_t, z_t) in real time.

IV. Results

A. Experiment Setup

In order to test the performance of the designed SPR, an experimental system is established, as shown in Fig. 4(a). This system consists of the following parts. The NI controller module (NI 9174; National Instruments, Austin, TX, USA) is used to communicate with the PC and three voltage output boards (NI 9263; National Instruments, Austin, TX, USA) for generating the low analog voltage sequence range from 0 to 5 V. In order to check whether the control voltage is correct during the experiment, a voltage acquisition module (USB-31110, Smacq Technologies. Co., Ltd., Beijing, China) is used to monitor the

$$\mathbf{T}_c(\boldsymbol{q}) = \begin{bmatrix}\cos^2\phi(\cos\theta - 1) + 1 & \sin\phi\cos\phi(\cos\theta - 1) & \cos\phi\sin\theta & \lambda\cos\phi(1 - \cos\theta)\\ \sin\phi\cos\phi(\cos\theta - 1) & \cos^2\phi(1 - \cos\theta) + \cos\theta & \sin\phi\sin\theta & \lambda\sin\phi(1 - \cos\theta)\\ -\cos\phi\sin\theta & -\sin\phi\sin\theta & \cos\theta & \lambda\sin\theta\\ 0 & 0 & 0 & 1\end{bmatrix}.$$

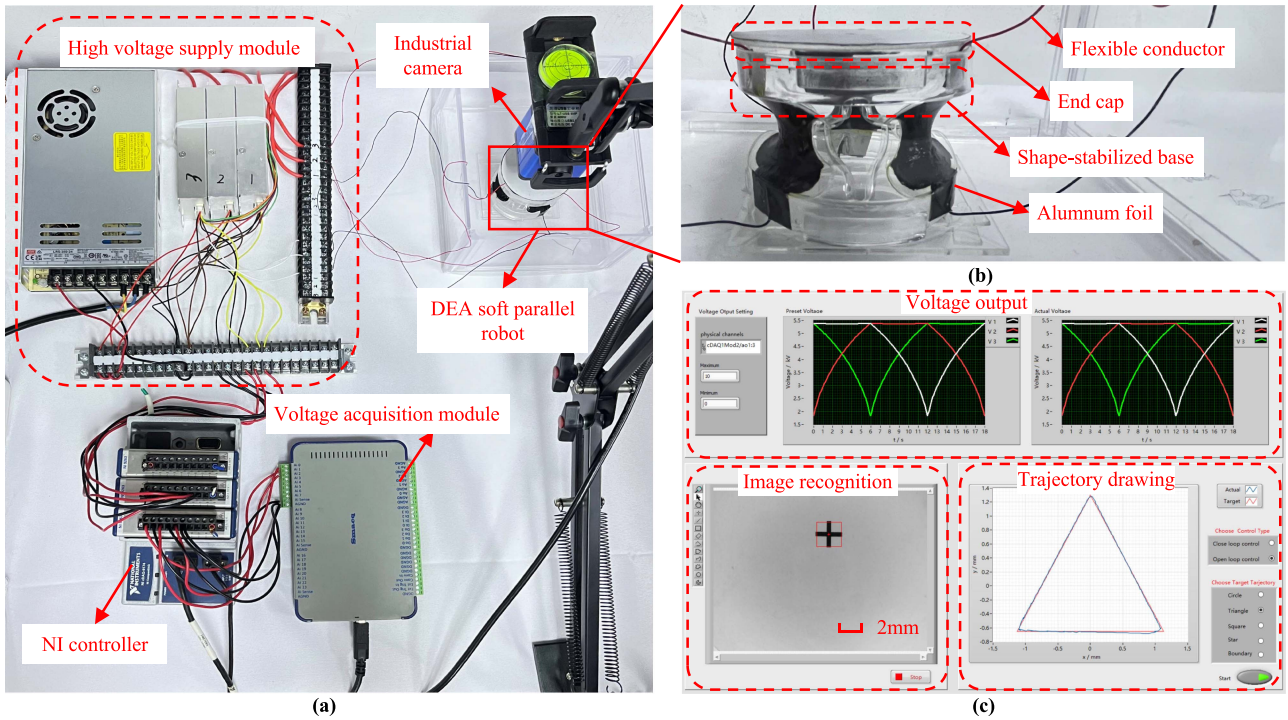

Fig. 4. Experiment Setup. (a) Robot system consists of the NI controller to generate the low analog voltage, a high-voltage supply module to amplify the low voltage to high control voltage, an industrial camera to capture the motion of the soft robot and a voltage acquisition module to measure the control voltage. (b) SPR with an end cap and two shape-stabilized bases and aluminum foil pasted. (c) Software consists of the voltage output chart, image recognition window, and the trajectory drawing chart.

voltage generated by the NI controller in real time. A high-voltage supply module (P103-1FU1, Dongwen High Voltage Power Supply Corp, Tianjin, China) is used to amplify (2000 times) the analog voltage generated by the NI controller to actuate the DEAs. Moreover, an industrial camera (LT-H8179, Qingdao Blue Sky Technology Co., Ltd., Qingdao, China) is used for capturing the motion of the robot.

Fig. 4(b) shows the SPR, two shape-stabilized bases, and an end cap. The flexible conductor is pasted on the two bases through aluminum foil. A small cross mark is designed on the end cap for image recognition and real-time motion display. Besides, we designed a front panel based on LABVIEW for operation and display, as shown in Fig. 4(c). The front panel consists of the voltage output chart to show the actual actuation voltage, an image recognition window to track the designed cross mark based on the template matching method, and a trajectory drawing chart to plot the actual and desired trajectories. To ensure the accuracy of the experiment, we adjusted the camera view, and the observable region is about 16 mm $\times$ 12 mm, while the resolution is 1600 $\times$ 1200, so the pixel accuracy is about 10 μm.

B. Stiffness Analysis

In this section, we test the axial stiffness and bending stiffness of the proposed SPR, respectively, as shown in Fig. 5(a). The digital force gauge (WD-2/0.2, Wenzhou WeDo Electronics Co., Ltd., Wenzhou, China) has a measuring range of $\pm$ 0.2 N and a measuring accuracy of $\pm 0.5\%$. Fig. 5(b) shows the bending stiffness of the SPR in different directions. The red, blue, yellow, and green curves represent the stress curves when the robot's edge is compressed by 2, 4, 6, and 8 mm. It can be seen that the forces in all directions are basically the same under the same compression, so the bending stiffness of the SPR is almost uniform in all directions. In order to further quantitatively analyze the bending stiffness of SPR, we chose two special directions, $\varphi = 90°$ and $\varphi = -90°$. As shown in Fig. 5(d), it can be seen that the curves are approximately straight, demonstrating that a proportional increment in force corresponds to an increase in edge compression.

Fig. 5(c) shows the relationship curves between the force and displacement in the process of compression and extension at the center of the SPR. It can be seen that the axial stiffness is greater than the bending stiffness by comparing with Fig. 5(d). The two curves closely resemble linear relationships, and the tensile and compressive stiffness are roughly equivalent. According to the least-square method, the axial stiffness of the robot is about 0.11 N/mm.

C. Training Result of the Neural Network Model

In this part, we train our neural network model with the collected dataset and plot relative results shown in Fig. 6. As mentioned previously, we use the neural network method for electromechanical modeling due to its excellent nonlinear fitting and generalization ability. In order to show the training accuracy,

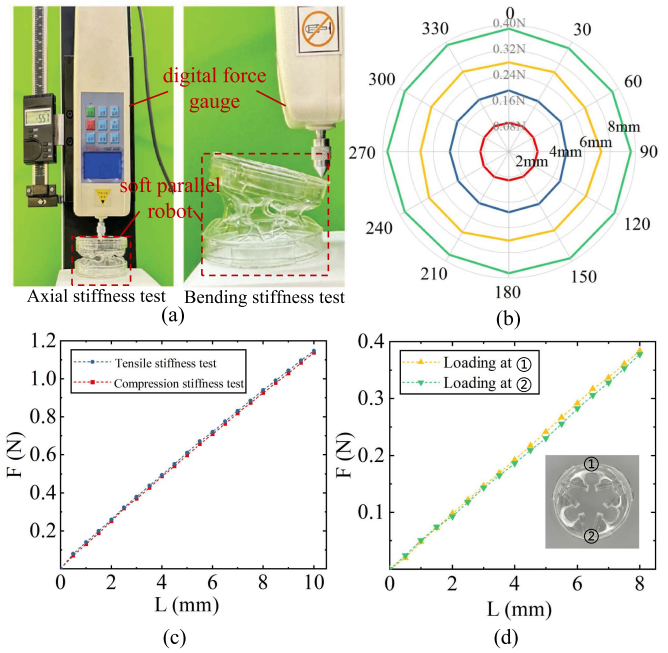

Fig. 5. (a) Stiffness Analysis experimental settings. (b) Bending stiffness analysis of the SPR in different directions. (c) Axial stiffness analysis of the SPR. (d) Bending stiffness analysis of the SPR in two special directions.

we plot several curves to show the relationship between the elongation and the actuation voltage [see Fig. 6(a)]. When the voltage is lower than 1 kV, there is no obvious elongation of the actuator. As the voltage gradually increases, the length of the actuator is also elongated gradually, and the elongation growth rate also increases. It is because the thickness of the DE membrane is getting smaller, and according to the deformation principle of the DEA mentioned previously, the stress of the DE membrane is increased. The target and output curves are almost coincident on the training set, validation set, and test set. To make the errors between curves more observable, Fig. 6(b) shows the error distribution curves of different datasets. The maximum error does not exceed 15 μm, and the large error mainly occurs in the initial stage of deformation as the elongation is less than 0.5 mm. When the elongation exceeds 0.5 mm, the error is greatly reduced and gradually stabilized within a small range.

In order to further analyze the predicted error of the neural network, we plot the error histogram with 20 bins [see Fig. 6(c)]. It is observed that more than 70% of errors are in the bin that less than 1μm. Besides, the curves in Fig. 6(d) also show that the neural network has great fitting accuracy with a regression coefficient of 0.9999. The overall results verify that the neural network could be able to learn the nonlinearity deformation of the SPR and establish a solid foundation for robot control.

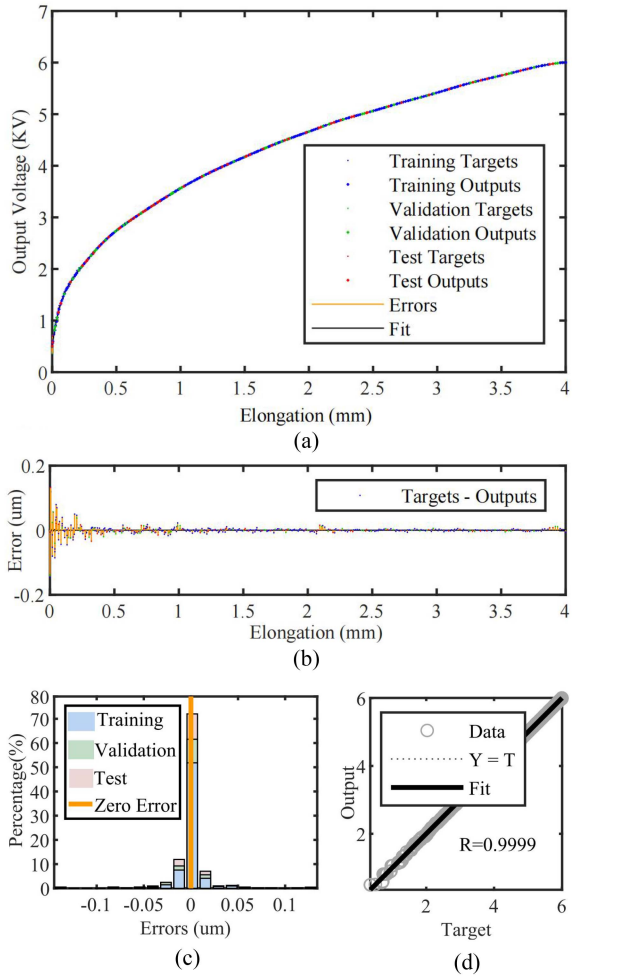

Fig. 6. Training result of the neural network. (a) Output voltage curves relative to elongation of different training sets. (b) Error distribution curves of different datasets. (c) Error distribution histogram. (d) Regression curve between target value and predicted value of neural network.

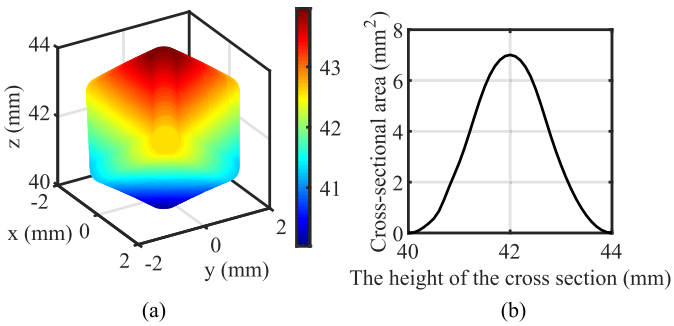

Fig. 7. Workspace analysis. (a) 3-D kinematic workspace of the SPR. (b) *Z*-axis cross-sectional area relative to the *Z*-axis height.

D. Workspace Analysis

In this subsection, we analyze the workspace of the robot based on the forward kinematics model. Under the maximum safe energization voltage of 6 kV, the SPR could reach the elongation of 4 mm with the original height of 40 mm (including the length of the two shape-stabilized bases). The initial height of the DE membrane is 20 mm, so the elongation rate is 20%. Taking the original length and the elongation of the DEA into the forward kinematics, we could obtain the workspace of the SPR, as shown in Fig. 7(a). The workspace volume is 12 mm^3. We also analyzed the *Z*-axis cross-sectional area relative to the

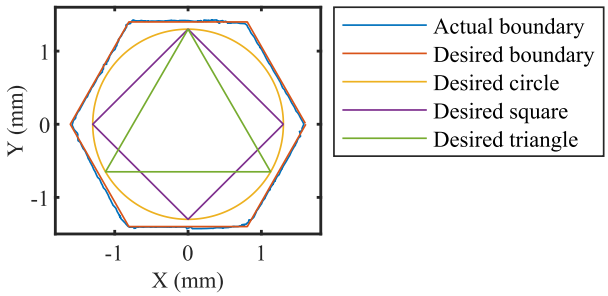

Fig. 8. Actual and desired boundary curves, and different trajectories within the boundary.

Z-axis height, as shown in Fig. 7(b). The results show that when the height is 42 mm, the section area is the largest at 6.8 mm^2, providing a theoretical guide to choosing the trajectory plane.

We design several different trajectories on the maximum cross section of the workspace, including triangle, circle, and square, shown in Fig. 8. We also carried out experiments to obtain the actual boundary and compared it with the target boundary. The results show that the two boundary curves almost coincide, verifying the accuracy of the proposed hybrid model.

E. Trajectory Tracking Performance

In Section III, a control strategy is proposed based on the hybrid model for the SPR. To evaluate the control accuracy, trajectory tracking experiments are carried out. The robot is controlled to track three patterns (see Fig. 8) at different speeds and under different loads. The three patterns have the same circumscribed circle with a radius of 1.3 mm. The starting point of the three trajectories is (0, 1.3 mm), and the movement direction is counterclockwise. During the experiments, a 2-D camera is used to capture the position of the robot center in real time. It is worth mentioning that the maximum inclination angle of the robot's upper plane is 0.0619 rad when moving along different trajectories. The origin length of the "cross" mark is 2 mm, so the maximum change in length caused by the inclination is about 0.00383 mm, which is almost negligible. Therefore, a 2-D camera can meet the accuracy requirements for trajectory tracking.

First, set the velocity to 0.375 mm/s without load, and the control voltage sequences are generated to actuate the DEAs. The experimental results are shown in Fig. 9(a), where the solid black line is the desired trajectory, and the green line is the actual trajectory. It can be seen that the two trajectories basically coincide, indicating that the robot has good motion performance at this velocity. The tracking error distribution is shown as a green bar in Fig. 9(d). The errors mainly source from two aspects. The first is the neural network model error and the assumption based on the constant curvature. The second is the fabrication error, which can be caused by different electrodeformation characteristics of the DE membrane and the uneven area and thickness of the hand-painted carbon grease electrode.

Next, the load capacity of the robot is tested. 14 and 21 g (4 times and 6 times the weight of robot) loads are installed, respectively, on the upper plane of the robot, and trajectory planning experiments are carried out for the three patterns. The results are shown in Fig. 9(b), where the black line is the desired trajectory, and the orange and purple lines are the actual trajectories with the load of 14 and 21 g, respectively. It can be seen that when the load changes, the robot's trajectory coincides with the preset trajectory, indicating that the increase in load does not reduce the robot's tracking performance. This is because the robot is designed in a parallel configuration. Compared with the serial robot, the stiffness is greater. Even under the external load, the robot can still produce preset deformation, indicating that the robot has a good load capacity.

Next, the control performance of the robot at different tracking velocities is also tested. The results are shown in Fig. 9(c), where the black line is the desired trajectory, and the red and blue lines are the actual trajectories with the velocity of 0.75 and 1.5 mm/s, respectively. It can be seen that when the velocity increases, the motion range of the robot becomes significantly smaller. As the tracking velocity of the robot increases gradually, the charging and discharging speed of the DEA increases. Due to the hysteresis of the DEA, the deformation of the robot cannot reach the preset goal in real time.

Finally, to quantitatively analyze the trajectory tracking error, the mean error and standard deviation are calculated and plotted in Fig. 9(d). When the speed of the robot is 0.375 mm/s without any additional load, the mean positioning error of different trajectories is 13.4–16.6 μm. When the external load increases, the error of the robot increases, but it still maintains a high positioning accuracy. With loads of 14 and 21 g at a speed of 0.375 mm/s, the mean errors are 14.8–17.6 and 15.9–18.2 μm, respectively. When there is no additional load, the mean errors of three trajectories with the velocity of 0.75 and 1.5 mm/s are 98.2–103.4 μm and 231.8–236.2 μm, respectively. It can be seen from Fig. 9(c) that although the range of the three trajectories becomes smaller, there is no significant distortion in shape.

F. Micromanipulation Experiment

To further verify the micromanipulation capability of the SPR, a microneedle is mounted in the upper plane of the robot, and zebrafish embryo puncture experiments are carried out, as depicted in Fig. 10. The puncture procedure includes the following steps: first, the SPR is controlled to bring the microneedle close to the zebrafish embryo; second, the surface of the embryo begins to deform after being touched by the microneedle; third, the microneedle advances until it penetrates the zebrafish embryo; and finally, the microneedle is withdrawn from the embryo and return to the initial position. The experimental results demonstrate that the proposed robot has high control accuracy and the potential for application in the field of micromanipulation.

G. Discussion

Compared with the conventional soft serial robots, the SPRs have great application prospects in micromanipulation, microassembly, and microsurgery due to their higher stiffness, greater load capacity, and higher precision. This work presents a lightweight (3.5 g) small-scale (ϕ60×40 mm) SPR made up

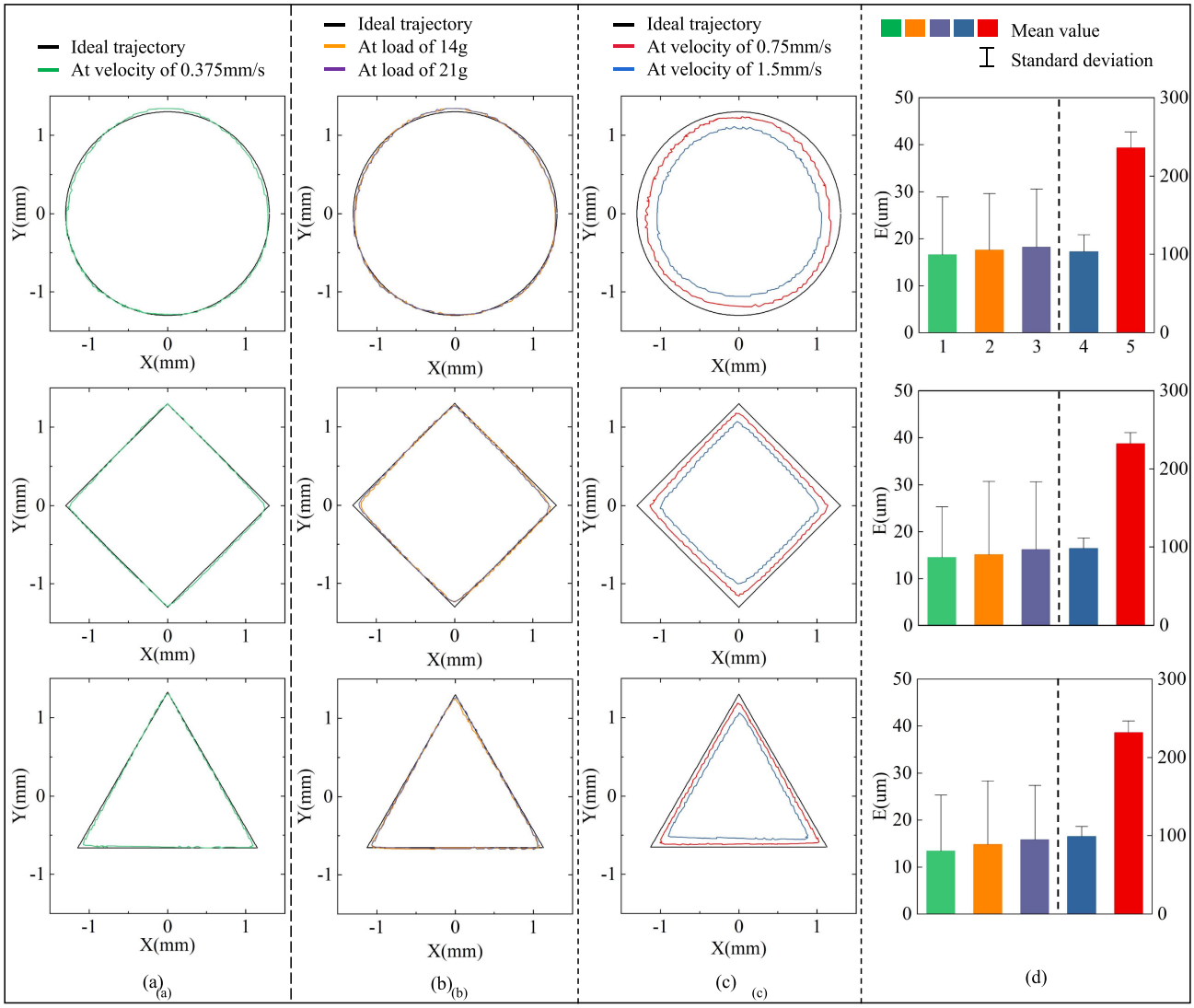

Fig. 9. Trajectory tracking experiments. (a) Tracking trajectory of circle, triangle, and square patterns at the velocity of 0.375 mm/s without load. (b) Tracking trajectory of circle, square, and triangle patterns at the velocity of 0.375 mm/s with the load of 14 and 21 g. (c) Tracking trajectory of circle, square, and triangle patterns at the velocity of 0.75 and 1.5 mm/s without load. (d) Tracking error distributions of circle, square, and triangle patterns, respectively, under different conditions [one-to-one correspondence with the same color in Fig. 9(a)–(c)].

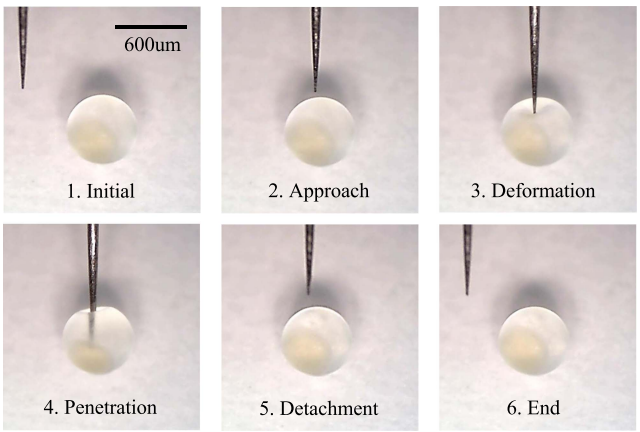

Fig. 10. Zebrafish embryo puncture experiments with the SPR.

of three symmetrically arranged DEAs and a lot of experiments have been carried out to analyze the performance of the robot. The results show that the robot has high control accuracy and the potential to be applied in the field of micromanipulation.

In order to further demonstrate the performance of robots, Table III shows the comparison between the proposed SPR and other existing SPRs. Few SPRs can achieve micron-level precision control. In terms of driving method: pneumatic SPRs often need to be equipped with multiple silicone chambers and solenoid valves, resulting in bulky and complex robot systems, and the response speed is usually limited by the ability to pump air in and out of the actuator [15], [32]; tendon-actuated SPRs are usually limited to planar motion for better control accuracy and need to occupy a large area [16], [33]; SMA-actuated SPRs are slow in response, and the temperature dependence makes it difficult to control [17], [34], [35]; DE-actuated SPRs

TABLE III
COMPARISON BETWEEN THIS WORK AND SOME SPRS

Reference	Link type	Size[1]	NOA[2]	Accuracy	Actuation method
SPR [15]	flexible	$\approx \phi$200×150mm	3	6.4-9.2cm	Pneumatic
Wrist rehabilitation robot [32]	flexible	$\approx \phi$100×440mm	6	——	Pneumatic
Extracorporeal ultrasound robot [37]	flexible	$\approx \phi$170×130mm	3	0.39mm	Pneumatic
Planar continuum robot [16]	flexible & rigid	$>\phi$580mm	3	1.8mm	Tendon-actuated
Reconfigurable continuum robot [33]	flexible	$>\phi$200mm	6	3.3mm	Tendon-actuated
Soft parallel Stewart platform [34]	flexible	$\approx \phi$170×90mm	6	——	SMA-actuated
Multi-DoF continuum robot [35]	flexible	ϕ80×345mm	9	1.42mm	SMA-actuated
Soft robotic arm [17]	flexible	ϕ26×80mm	3	0.16mm	SMA-actuated
Bionic eyeball motion actuator [19]	flexible	$\approx \phi$50×150mm	3	1.086-1.719mm	DE-actuated
Drawing robot [18]	flexible	$\approx\phi$200×160mm	3	——	DE-actuated
Cone actuator [36]	flexible & rigid	ϕ60×50mm	8	±4.45 mm	DE-actuated
ours	**flexible**	$\boldsymbol{\phi}$**60×40mm**	**3**	**13.4-16.6**μm	**DE-actuated**

[1] The overall size not clearly provided in the literature is estimated based on the scale and the given size.
[2] NOA: Number of actuators.

have fast response speed and compact structure. However, the existing DE-actuated SPRs need to be equipped with additional structures inside for support and restoration, such as spring [19] and connecting rod [36], which increases the weight of the robot and limits its application. Moreover, an integrated design and manufacturing method is proposed. The actuators can be fabricated and assembled simultaneously rather than fabricating several actuators individually, and then, assembling them with connectors. The integrated method overcomes the limitations of conventional manufacturing methods, take advantage of lower material costs and processing time costs, reduces processing errors, endows the robot with a compact structure and ultra-lightweight mass, and lays the foundation for high-precision positioning.

This study opens up a new path for the design and control of the soft lightweight small-scale parallel robot with high-precision positioning. In the future, the closed-loop control of the robot will be further studied to compensate for the inevitable errors in manufacturing and modeling.

V. CONCLUSION

Due to the great application potential in the industrial production and biomedical field, this article proposed a DE-actuated soft lightweight small-scale parallel robot. With the integrated design and fabrication strategy, the robot has a compact structure, low manufacturing cost, and a simplified manufacturing process. A hybrid-model-based open-loop controller is established, and the proposed robot achieves high trajectory tracking accuracy. The average positioning error of the different trajectories is 13.4–16.6 μm. The zebrafish embryo puncture experiments have proved that the robot has micromanipulation capabilities.

REFERENCES

[1] V. Gough, "Contribution to discussion to papers on research in automobile stability and control and in tire performance," *Proc. Automot. Division Inst. Mech. Eng.*, vol. 180, pp. 392–394, 1957.
[2] V. E. Gough, "Universal tyre test machine," in *Proc. FISITA 9th Int. Tech. Congr.*, London, U.K., 1962, pp. 117–137.
[3] H. McClintock, F. Z. Temel, N. Doshi, J.-s. Koh, and R. J. Wood, "The milidelta: A high-bandwidth, high-precision, millimeter-scale delta robot," *Sci. Robot.*, vol. 3, no. 14, 2018, Art. no. eaar3018.
[4] F. Pierrot, C. Reynaud, and A. Fournier, "Delta: A simple and efficient parallel robot," *Robotica*, vol. 8, no. 2, pp. 105–109, 1990.
[5] W. Xu, J.-S. Pap, and J. Bronlund, "Design of a biologically inspired parallel robot for foods chewing," *IEEE Trans. Ind. Electron.*, vol. 55, no. 2, pp. 832–841, Feb. 2008.
[6] S. Briot, A. Pashkevich, and D. Chablat, "Optimal technology-oriented design of parallel robots for high-speed machining applications," in *Proc. IEEE Int. Conf. Robot. Automat.*, 2010, pp. 1155–1161.
[7] J. Mo, Z.-F. Shao, L. Guan, F. Xie, and X. Tang, "Dynamic performance analysis of the x4 high-speed pick-and-place parallel robot," *Robot. Comput.- Integr. Manuf.*, vol. 46, pp. 48–57, 2017.
[8] Z. Li, X. Li, Q. Li, H. Su, Z. Kan, and W. He, "Human-in-the-loop control of soft exosuits using impedance learning on different terrains," *IEEE Trans. Robot.*, vol. 38, no. 5, pp. 2979–2993, Oct. 2022.
[9] W. He, C. Xue, X. Yu, Z. Li, and C. Yang, "Admittance-based controller design for physical human–robot interaction in the constrained task space," *IEEE Trans. Automat. Sci. Eng.*, vol. 17, no. 4, pp. 1937–1949, Oct. 2020.
[10] T. Xu, Z. Hao, C. Huang, J. Yu, L. Zhang, and X. Wu, "Multimodal locomotion control of needle-like microrobots assembled by ferromagnetic nanoparticles," *IEEE/ASME Trans. Mechatron.*, vol. 27, no. 6, pp. 4327–4338, Dec. 2022.
[11] J. Zhang et al., "A survey on design, actuation, modeling, and control of continuum robot," *Cyborg Bionic Syst.*, vol. 2022, 2022, Art. no. 9754697.
[12] C. Laschi, B. Mazzolai, and M. Cianchetti, "Soft robotics: Technologies and systems pushing the boundaries of robot abilities," *Sci. Robot.*, vol. 1, no. 1, 2016, Art. no. eaah3690.
[13] D. Liu et al., "Magnetically driven soft continuum microrobot for intravascular operations in microscale," *Cyborg Bionic Syst.*, vol. 2022, 2022, Art. no. 9850832.
[14] I. L. Sander, N. Dvorak, J. A. Stebbins, A. J. Carr, and P.-A. Mouthuy, "Advanced robotics to address the translational gap in tendon engineering," *Cyborg Bionic Syst.*, vol. 2022, 2022, Art. no. 9842169.
[15] X. Huang, X. Zhu, and G. Gu, "Kinematic modeling and characterization of soft parallel robots," *IEEE Trans. Robot.*, vol. 38, no. 6, pp. 3792–3806, Dec. 2022.
[16] K. Nuelle, T. Sterneck, S. Lilge, D. Xiong, J. Burgner-Kahrs, and T. Ortmaier, "Modeling, calibration, and evaluation of a tendon-actuated planar parallel continuum robot," *IEEE Robot. Automat. Lett.*, vol. 5, no. 4, pp. 5811–5818, Oct. 2020.
[17] H. Yang, M. Xu, W. Li, and S. Zhang, "Design and implementation of a soft robotic arm driven by SMA coils," *IEEE Trans. Ind. Electron.*, vol. 66, no. 8, pp. 6108–6116, Aug. 2019.
[18] C. Jiang et al., "Flexible parallel link mechanism using tube-type dielectric elastomer actuators," *J. Robot. Mechatron.*, vol. 27, no. 5, pp. 504–512, 2015.
[19] L. Li, H. Godaba, H. Ren, and J. Zhu, "Bioinspired soft actuators for eyeball motions in humanoid robots," *IEEE/ASME Trans. Mechatron.*, vol. 24, no. 1, pp. 100–108, Feb. 2019.
[20] R. J. Webster III and B. A. Jones, "Design and kinematic modeling of constant curvature continuum robots: A review," *Int. J. Robot. Res.*, vol. 29, no. 13, pp. 1661–1683, 2010.
[21] I. S. Godage, G. A. Medrano-Cerda, D. T. Branson, E. Guglielmino, and D. G. Caldwell, "Modal kinematics for multisection continuum arms," *Bioinspiration Biomimetics*, vol. 10, no. 3, 2015, Art. no. 035002.

[22] P. S. Gonthina, A. D. Kapadia, I. S. Godage, and I. D. Walker, "Modeling variable curvature parallel continuum robots using euler curves," in *Proc. Int. Conf. Robot. Automat.*, 2019, pp. 1679–1685.
[23] W. McMahan, B. A. Jones, and I. D. Walker, "Design and implementation of a multi-section continuum robot: Air-octor," in *Proc. IEEE/RSJ Int. Conf. Intell. Robots Syst.*, 2005, pp. 2578–2585.
[24] F. Janabi-Sharifi, A. Jalali, and I. D. Walker, "Cosserat rod-based dynamic modeling of tendon-driven continuum robots: A tutorial," *IEEE Access*, vol. 9, pp. 68703–68719, 2021.
[25] M. M. Dalvand, S. Nahavandi, and R. D. Howe, "An analytical loading model for n-tendon continuum robots," *IEEE Trans. Robot.*, vol. 34, no. 5, pp. 1215–1225, Oct. 2018.
[26] G. Fang, Y. Tian, Z.-X. Yang, J. M. Geraedts, and C. C. Wang, "Efficient Jacobian-based inverse kinematics with sim-to-real transfer of soft robots by learning," *IEEE/ASME Trans. Mechatron.*, vol. 27, no. 6, pp. 5296–5306, Dec. 2022.
[27] Z. Geng and L. Haynes, "Neural network solution for the forward kinematics problem of a stewart platform," in *Proc. IEEE Int. Conf. Robot. Automat.*, 1991, pp. 2650–2651.
[28] T. Lu, C. Ma, and T. Wang, "Mechanics of dielectric elastomer structures: A review," *Extreme Mechanics Lett.*, vol. 38, 2020, Art. no. 100752.
[29] Y. Li, I. Oh, J. Chen, H. Zhang, and Y. Hu, "Nonlinear dynamic analysis and active control of visco-hyperelastic dielectric elastomer membrane," *Int. J. Solids Struct.*, vol. 152, pp. 28–38, 2018.
[30] Z. Suo, "Theory of dielectric elastomers," *Acta Mechanica Solida Sinica*, vol. 23, no. 6, pp. 549–578, 2010.
[31] M. Wissler and E. Mazza, "Electromechanical coupling in dielectric elastomer actuators," *Sensors Actuators A, Phys.*, vol. 138, no. 2, pp. 384–393, 2007.
[32] Y. Wang and Q. Xu, "Design and testing of a soft parallel robot based on pneumatic artificial muscles for wrist rehabilitation," *Sci. Rep.*, vol. 11, no. 1, 2021, Art. no. 1273.
[33] G. Böttcher, S. Lilge, and J. Burgner-Kahrs, "Design of a reconfigurable parallel continuum robot with tendon-actuated kinematic chains," *IEEE Robot. Automat. Lett.*, vol. 6, no. 2, pp. 1272–1279, Apr. 2021.
[34] E. L. White, J. C. Case, and R. Kramer-Bottiglio, "A soft parallel kinematic mechanism," *Soft Robot.*, vol. 5, no. 1, pp. 36–53, 2018.
[35] C. Cheng, J. Cheng, and W. Huang, "Design and development of a novel SMA actuated multi-DOF soft robot," *IEEE Access*, vol. 7, pp. 75073–75080, 2019.
[36] A. T. Conn and J. Rossiter, "Towards holonomic electro-elastomer actuators with six degrees of freedom," *Smart Mater. Struct.*, vol. 21, no. 3, 2012, Art. no. 035012.
[37] L. Lindenroth, R. J. Housden, S. Wang, J. Back, K. Rhode, and H. Liu, "Design and integration of a parallel, soft robotic end-effector for extracorporeal ultrasound," *IEEE Trans. Biomed. Eng.*, vol. 67, no. 8, pp. 2215–2229, Aug. 2020.

Qin Fang received the M.S. degree in aircraft design in 2021 from the School of Aeronautics and Astronautics, Zhejiang University, Hangzhou, China, where she is currently working toward the Ph.D. degree in control science and engineering with the Department of Control Science and Engineering.

Her research interests include soft robots, small-scale robots, and bionic robots.

Jingyu Zhang received the M.S. degree in mechanical manufacturing in 2021 from the School of Mechanical Engineering, Zhejiang University, Hangzhou, China, where he is currently working toward the Ph.D. degree in control science and engineering with the Department of Control Science and Engineering.

His research interests include medical robots and soft continuum robots.

Danying Sun received the B.Eng. degree in automation from the Nanjing University of Science and Technology, Nanjing, China, in 2020. She is currently working toward the M.S. degree in control science and engineering with the Department of Control Science and Engineering, Zhejiang University, Hangzhou, China.

Her research interests include soft magnetic robots and untethered sensing systems.

Yanan Xue received the M.D. degree in plastic surgery from the Zhejiang University School of Medicine, Hangzhou, China, in 2023.

She is currently working with the Plastic Surgery Department, Zhejiang Provincial People's Hospital and the Department of Control Science and Engineering, Zhejiang University, Hangzhou. Her research interests include micromedical robots, tissue regeneration repair, and scar treatment.

Rui Jin received the B.E. degree in mechanical design, manufacturing, and automation from Northwestern Polytechnical University, Xian, China, in 2021. He is currently working toward the M.S. degree in control science and engineering with the Department of Computer Science and Technology, Zhejiang University, Hangzhou, China.

His research interests include coaxial helicopters and autonomous flight.

Nenggan Zheng (Senior Member, IEEE) received the B.E. degree in biomedical engineering and the Ph.D. degree in computer science, both from Zhejiang University, Hangzhou, China, in 2002 and 2009, respectively.

He is currently a Professor with the Department of Computer Science and Technology, Zhejiang University. His research interests include artificial intelligence, software engineering, and electronic engineering.

Yue Wang (Member, IEEE) received the Ph.D. degree in control science and engineering from the Department of Control Science and Engineering, Zhejiang University, Hangzhou, China, in 2016.

He is currently an Associate Professor with the Department of Control Science and Engineering, Zhejiang University. His research interests include mobile robotics and robot perception.

Rong Xiong (Member, IEEE) received the Ph.D. degree in control science and engineering from the Department of Control Science and Engineering, Zhejiang University, Hangzhou, China, in 2009.

She is currently a Professor with the Department of Control Science and Engineering, Zhejiang University. Her research interests include motion planning and SLAM.

Zhefeng Gong received the Ph.D. degree in biophysics from the Institute of Biophysics, Chinese Academy of Sciences, Beijing, China, in 2000.

He is currently a Professor with the Medical School of Zhejiang University, Hangzhou, China. His research interest includes sensorimotor transformation in animals and neural control of animal movements.

Haojian Lu (Member, IEEE) received the B.Eng. degree in mechatronical engineering from the Beijing Institute of Technology, Beijing, China, in 2015, and the Ph.D. degree in robotics from the City University of Hong Kong, Kowloon, Hong Kong, in 2019.

He is currently a Professor with the State Key Laboratory of Industrial Control and Technology, and the Institute of Cyber-Systems and Control, Zhejiang University, Hangzhou, China. His research interests include micro/nanorobotics, bioinspired robotics, medical robotics, micro aerial vehicle, and soft robotics.